Tidal and atmospheric influences on near-surface turbulence in an estuary

Philip M. Orton,[1,2,3] Christopher J. Zappa,[1] and Wade R. McGillis[1,4]

Received 30 March 2010; revised 13 September 2010; accepted 1 October 2010; published 14 December 2010.

[1] Estuarine near-surface turbulence is important for transport, mixing, and air-water exchanges of many important constituents but has rarely been studied in detail. Here, we analyze a unique set of estuarine observations of in situ atmospheric and full water column measurements, estimated air-sea exchanges, and acoustic measurements of several terms in the turbulent kinetic energy (TKE) budget. Observations from a 5.1 m deep site in the Hudson River estuary include dissipation at 50 cm depth (ε_{50}), as well as profiles of TKE, shear production of TKE (P), and net turbulent vertical TKE transport (T_D). Regressions suggest that the principal controlling factor for ε_{50} was wind (through the surface shear velocity, U_*) and that the surface heat flux and tidal currents played a secondary role. For ebb spring tides, the TKE budget at 50 cm depth was closed within noise levels. Ebbs had high ε_{50} due to local shear production, which nearly balanced ε_{50}. Floods had T_D approaching P in the upper water column but generally weak near-surface shear and turbulence. Examining buoyancy fluxes that impact near-surface stratification and can indirectly control turbulence, solar heat input and tidal straining caused similar buoyancy fluxes on a sunny, calm weather day, promoting ebb tide restratification. Wind-driven mixing was found to dominate during a fall season storm event, and strong overnight heat loss after the storm helped delay restratification afterward. These results demonstrate the utility of combining detailed air-sea interaction and physical oceanographic measurements in future estuary studies.

Citation: Orton, P. M., C. J. Zappa, and W. R. McGillis (2010), Tidal and atmospheric influences on near-surface turbulence in an estuary, *J. Geophys. Res.*, *115*, C12029, doi:10.1029/2010JC006312.

1. Introduction

[2] Turbulent mixing in the upper water column of the coastal ocean, in contrast to its well-known neighbor bottom boundary layer mixing, is not well understood and presents difficulties for observations and numerical modeling. One of the primary remaining shortcomings of coastal and estuarine three-dimensional numerical models is that the upper water column density structure is poorly predicted, likely as a consequence of inaccurate mixing parameterizations [*Li et al.*, 2005; *Souza et al.*, 2008; *Warner et al.*, 2005]. These deficiencies have typically led to reduced skill in predicting spatial density gradients and circulation [*Li et al.*, 2005; *Warner et al.*, 2005].

[3] Near-surface turbulence in the upper few meters of estuaries and the coastal ocean is also important for constituent transport. This is especially the case for surface oriented pollutants such as oil slicks or contaminants transported in buoyant freshwater in combined sewer overflows; biological particles such as plankton, which can often only grow in surface estuarine waters because of light limitation by turbidity [*Malone*, 1977]; and fine sediments and particle-associated pollutants that arrive in the estuary in buoyant river water and have a nonlinear response to turbulent mixing (and thus, increasing salinity) because it facilitates particle aggregation and sedimentation. There is a strong role for near-surface turbulence for constituents with fluxes across the air-water interface in a gaseous phase (e.g., oxygen, carbon dioxide, PCBs), because turbulence near the sea surface governs gas transfer [*Zappa et al.*, 2007].

[4] Estuaries are highly diverse in terms of stratification, wind fetch, tidal range and depth, as well as many other factors. As a result, in some cases near-surface turbulence will have similarity to lakes, rivers, or the open ocean. In the open ocean, processes resulting from wind forcing such as direct wind-driven shear, wave breaking [e.g., *Gemmrich and Farmer*, 2004] or Langmuir circulation [e.g., *Gargett and Wells*, 2007] are often dominant. In lakes, the surface heat flux is an important factor for turbulence, with seasonal or diurnal convective overturning [*Imberger*, 1985]. In rivers and strongly forced, unstratifed systems, near-surface tur-

[1]Lamont-Doherty Earth Observatory of Columbia University, Palisades, New York, USA.
[2]Earth and Environmental Science, Columbia University, New York, New York, USA.
[3]Now at Stevens Institute of Technology, Hoboken, New Jersey, USA.
[4]Earth and Environmental Engineering, Columbia University, New York, New York, USA.

0148-0227/10/2010JC006312

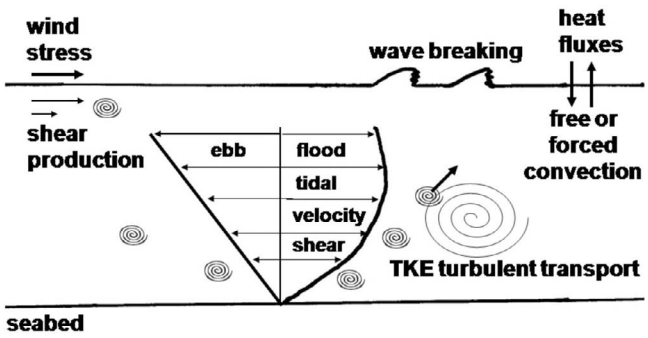

Figure 1. Conceptual diagram showing some of the processes that may influence upper water column turbulence in a partially mixed or salt wedge estuary. Vectors at the center show characteristic ebb tide (toward the left) and flood tide (toward the right) velocity profiles.

bulence is mainly related to water speed and depth. Even in 30 m depth waters in the North Sea, large-scale coherent turbulent flow structures have been observed to reach the water surface, and *Nimmo Smith et al.* [1999] present evidence that dispersion of materials due to currents is greater than dispersion due to Langmuir circulation when the water speed is greater than ~2% of the wind speed. In an unstratified laboratory open channel flow, *Hurther et al.* [2007] found that vertical turbulent transport (Figure 1) of turbulent kinetic energy (TKE) due to large coherent stress structures generated in the wall layer controls turbulence at heights above 80% of the boundary layer height. Last, in many cases, stratification will be important, but can have complex effects due to its impact of damping turbulence but also accompanying and promoting enhanced shear on ebb tides: a recent estuarine study showed that stratification could reduce turbulence to well below wall layer predictions during neaps, but increase it above those levels through local shear instability in the middle of the water column during spring tides [*Peters and Bokhorst*, 2000].

[5] Our ability to observe and understand near-surface turbulence in natural water bodies has been limited by several factors, including (1) the fact that it is often highly heterogeneous in space and time, (2) it can be too subtle to be measured by conventional instruments, (3) it is in a moving reference frame with tides and waves displacing the sea surface, and (4) the turbulent velocity fluctuations of interest are much smaller than surface wave orbitals. Observations of turbulent mixing far from the bottom boundary have until recently required costly and labor-intensive instrumentation. Turbulence near the sea surface is also complicated by processes occurring at the air-water interface that are difficult to measure, such as wave breaking and heat fluxes.

[6] A study was designed with the overriding goals of (1) studying the influence of water column and atmospheric processes on near-surface turbulence in an estuary and (2) demonstrating a framework for making autonomous (long-term, continuous) measurements of these processes that capture the breadth of their heterogeneity. The study utilized surface- and bottom-based autonomous measurement platforms and a combination of small-scale and large-scale turbulent velocity measurements with acoustic velocity sensors, which are relatively insensitive to calibration drift and biofouling. A bottom-mounted acoustic Doppler current profiler (ADCP) was used for measuring velocity of the mean flow field and the larger turbulent motions. An acoustic Doppler velocimeter (ADV) on an anchored catamaran was used for observing small-scale motions relevant to the TKE dissipation near the sea surface, and separating these motions from wave velocities through spectral analysis.

[7] This paper begins with a review of aspects of the TKE budget, and then describes the measurement campaign on the Hudson River estuary that included acoustic velocity and turbulence observations, as well as detailed meteorological measurements, full water column density time series, spatial density transects, and estimates of the net air-sea heat flux. The forcing of TKE dissipation at 50 cm depth (ε_{50}) is examined from the air and water side through regressions and dynamical analyses. Additionally, the drivers of near-surface ε are examined from a different perspective, by quantifying the sources and sinks in the TKE budget for periods when winds are below 3 m s^{-1}. The paper concludes by considering the indirect role of factors that can influence stratification such as tidal straining or surface heat fluxes.

2. Background

[8] The most common way that turbulence is generated in the coastal ocean is through conversion of kinetic energy of the mean flow into turbulent kinetic energy (TKE) by shear-driven instabilities. This energy flux from the mean flow field (e.g., $\overline{u}$) to the turbulent flow field (e.g., u') is referred to as shear production of TKE (P). A turbulent cascade has been theoretically and observationally shown to exist, where turbulent vortices interact and larger ones split into successively smaller ones. The vortices become smaller and smaller until they reach the scale at which they dissipate into heat due to molecular viscosity. The scales over which this occurs is called the inertial subrange, which spans the scale of the large eddies, roughly the scale of the shear layer depth, down to the scale of the smallest eddies where molecular viscosity causes dissipation.

[9] This energy flux from turbulent kinetic energy to heat is known as TKE dissipation (ε). TKE dissipation has been studied widely not only because it is important for turbulence energetics, but also for interdisciplinary reasons. It is valuable for understanding turbulent constituent fluxes, since these fluxes are roughly proportional to ε [*Rippeth et al.*, 2005]. It also is a useful variable for studying biological oceanography, because small-scale turbulence plays an important role in many of the life processes of many planktonic organisms (e.g., food, nutrient or predator encounters).

[10] If waters are vertically stratified with differing densities, not all turbulent kinetic energy that is produced runs through the turbulent cascade and is converted to heat. Instead, a small percentage of the TKE is expended in mixing water of differing densities, moving denser water upward and lighter water downward. This negative buoyancy flux increases the potential energy of the water column, so the TKE has been converted to potential energy, and energy is still conserved. Typically in the stratified portion of the water column, 5–20% of the TKE from shear production is expended through a buoyancy flux, and the remainder through dissipation [*Peters*, 1999]. Alternatively, processes such as

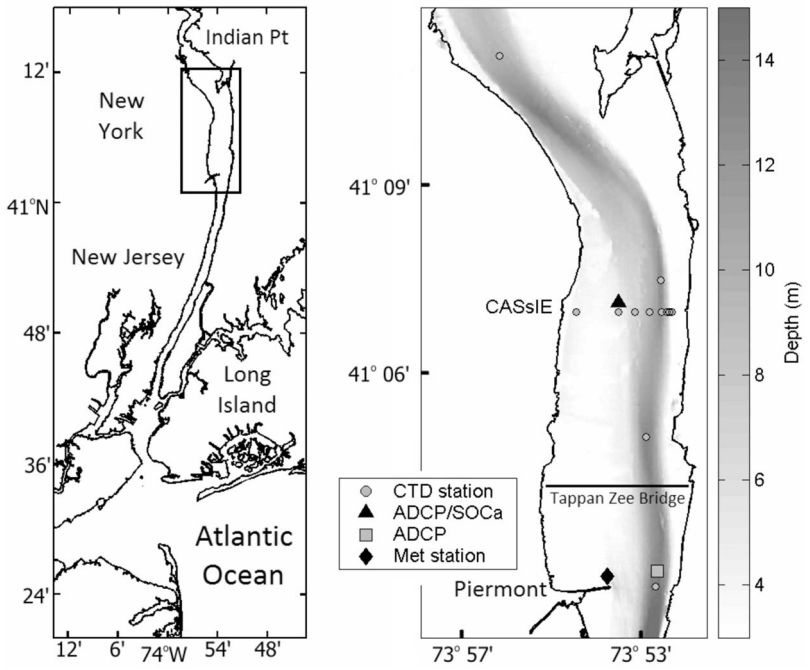

Figure 2. (left) The Hudson River estuary with (right) a zoom in to the 2007 CASsIE study site with shaded NOAA National Ocean Service bathymetry data. The self-orienting Catamaran (SOCa) was deployed at a mean depth of 5.1 m, 100 m south of the ADCP for the CASsIE study, and the meteorological (met) station was on Piermont Pier. Data from a 2004 ADCP deployment in 15 m depth water across from Piermont Pier are also used for comparison to the observed conditions during CASsIE.

evaporation or surface cooling can cause near-surface water to become negatively buoyant, and the convective movement of this water to a more stable position is also a buoyancy flux. This positive buoyancy flux can also be a source of TKE, a process often referred to as buoyancy production of TKE.

[11] Assuming horizontal spatial uniformity and a negligible vertical mean velocity, the TKE budget is

$$\frac{\partial \mathrm{TKE}}{\partial t} = P + B - \varepsilon + T_D + T_p \tag{1}$$

Here, the time-derivative of TKE per unit mass is on the left-hand side, where TKE = $1/2(\overline{u'^2} + \overline{v'^2} + \overline{w'^2})$, where bars are time averages and primes are perturbations from the mean. TKE shear production is $P = -\overline{u'w'}\partial U/\partial z - \overline{v'w'}\partial V/\partial z$; U, V, and W and u', v', and w' are mean and turbulent velocities from a Reynolds decomposition; the buoyancy flux is $B = -(g/\rho_0)\overline{w'\rho'}$; the dissipation rate of TKE is ε; the TKE transport due to turbulent pressure fluctuations (T_p) is typically considered to be negligible, and the net turbulent vertical transport of TKE is the divergence of the vertical turbulent flux of TKE, $T_D = \partial/\partial z(\overline{-w'\mathrm{TKE}})$. Order of magnitude estimates of T_D and ∂TKE/∂t in the ocean interior are similar to P and ε on short timescales (seconds to minutes) but much smaller when averaged over longer timescales [*Tennekes and Lumley*, 1972]. As a result, T_D and ∂TKE/∂t are often assumed to be negligible over the long averaging or time step periods in observational and modeling studies of turbulent mixing. Two-equation turbulent models (e.g., Mellor-Yamada, $k-\varepsilon$, $k-\omega$) are utilized widely for ocean circulation or coastal ocean numerical modeling, and typically represent the terms T_D and T_p jointly using a Fickian gradient diffusion model [*Scully et al.*, 2010; *Warner et al.*, 2005].

3. Methods

3.1. Field Experiments

[12] The Hudson River has a microtidal to mesotidal estuary, dominant semidiurnal tide, and a mean river input of 430 m^3 s^{-1} from the upper watershed north of Troy (1984–2008 average). The estuary and study area are shown in Figure 2. The brackish section of the estuary is typically 45–110 km long, yet with typical peak velocities of ~1 m s^{-1} [*Orton and Visbeck*, 2009], the tidal excursion during a flood or ebb tide is only ~10 km. The region of the estuary from Piermont Pier to Indian Point has been studied less than the narrower, more channelized region to the south. The study area is 3.6 km wide, has relatively low ship traffic and is ideal for studying a range of estuarine processes such as interacting wind-, wave-, and tide-forced currents, as well as deep channel (15 m depth) and shallow shoal (3–6 m depth) estuarine flows.

[13] An experiment referred to as CASsIE (Carbon and Air-Sea Interaction in an Estuary) was conducted at a 5 m deep shoal site along a broad region of the Hudson River estuary (Figure 2). The shoal site was chosen near the center of the estuarine cross section to have a large fetch in either direction and several miles north of the Tappan Zee Bridge to avoid contamination of air-sea CO_2 exchange measurements. A small self-orienting Catamaran (SOCa) [*Orton*,

2010; *Orton et al.*, 2010b] was anchored at this site over the period 23 September to 2 November 2007 (year days 265–303), to provide a surface-based view of turbulence, wind, and air-sea heat fluxes. Nearby, a bottom-mounted 1200 kHz acoustic Doppler current profiler (ADCP) measured vertical profiles of velocity, acoustic backscatter, and several turbulence parameters over year days 261–286 (see section 3.4). TRDI's rapid sampling mode 12 was used to record one ensemble average every second, an average of 21 subpings that were collected over 0.63 s (30 ms intervals). The vertical cell size was 0.25 m, and the resulting manufacturer estimate of velocity standard error for each ensemble average is 2.7 cm s^{-1}. Four 12 h anchor stations and a few truncated ones (by foul weather), two along- and four across-channel transects were also conducted with a small boat and CTD profiling to observe density stratification (locations in Figure 2). A CTD was attached to the ADCP frame, and temperature probes along the SOCa anchor line, for continuous time series measurements. A meteorological station was set up at Piermont Pier (Figure 2), 8 km to the south, and these data were used to validate and supplement the SOCa data sets. Piermont measurements included solar radiation, which helped estimate the net water-to-air heat flux (section 3.6).

[14] SOCa is an innovative platform useful for studying near-surface physical oceanography and air-sea interaction, with the name reflecting the fact that its keel rotates the vessel's instrumented boom into the current, so that measurements are never made in the wake. SOCa held an acoustic Doppler velocimeter (ADV) to measure near-surface currents and turbulent kinetic energy dissipation at 0.5 m depth, a sonic anemometer for wind velocity and temperature measurements at 1.2 m height, an inertial sensor to monitor platform motion, a water temperature probe at 0.5 m depth, and Licor LI-840 sensors for measuring CO_2 and H_2O concentrations and air-sea CO_2 fluxes. Single-height measurements of wind velocity, temperature and humidity, along with water velocity and temperature were used to compute bulk air-sea gradients, which were used with the COARE 3.0 bulk flux toolbox in Matlab [*Fairall et al.*, 2003] to estimate momentum and heat fluxes, wind stress, and the effective neutral wind velocity at 10 m height (U_{10N}). A detailed summary of the instrument platform and evaluation of its measurements during CASsIE is given by *Orton et al.* [2010b].

[15] An additional 15 m depth "channel site" ADCP data set from a 2004 deployment 7.5 km to the south (Figure 2) is utilized in this study for contrast against spring tide turbulence observed at the 5 m deep CASsIE shoal site. In 101 days of data collection, ensemble averages were recorded at 0.5 Hz, with vertical cell sizes of 0.5 m and standard error of 1.5 cm s^{-1}. These data are described in greater detail by *Orton and Visbeck* [2009].

[16] A moderately wide range of ambient conditions was covered during CASsIE (Figure 3). The period had ranges in 10 min averages of neutral equivalent 10 m height wind from 0 to 14.4 m s^{-1}, water depth from 4.7 to 6.2 m, surface water speed from 0 to 0.80 m s^{-1}, salinity from 5.5 to 16, air temperature from 6 to 32°C, water temperature from 17 to 25°C, and significant wave height from 0 to ~0.5 m. The top-to-bottom vertical salinity difference (ΔS; Figure 3f) was from 0 to 3.5, and local stratification ($\partial\rho/\partial z$) was from 0 to 4 kg m^{-4}. The peak stratification value came at a sharp pycnocline (2 kg m^{-3} over 0.5 m distance), but stratification was typically not this strong: it was below 1 kg m^{-4} for 98% of the measurements. Daily mean Hudson freshwater input from the upper watershed varied from 80 to 760 m^3 s^{-1} (measured at Green Island), corresponding to a range from mild drought conditions through most of the study to a moderately high flow rate just prior to the end of the period. The estimated net water-to-air heat flux ranged from −710 to 620 W m^{-2}, corresponding to a range from warm sunny days to very cold dry air mornings with surface waters 12°C warmer than the overlying air (methods described in section 3.6).

3.2. Acoustic Data Processing

[17] ADCP and ADV velocity data were bin-averaged in 10 min intervals. ADCP data were rotated from the earth reference frame into the direction of maximum near-bed velocity variance, to an along-stream (x) and across-stream (y) orthogonal reference frame. Data from the upper 6–8% of the water column were omitted, a standard procedure required because of acoustic sidelobe reflections off the sea surface, so velocity data are available from 1.25 m above the bed to ~0.3 m below the sea surface. ADV velocity data collected aboard SOCa are already oriented into the along-stream and across-stream directions for the surface current, due to the platform self-orienting capability [*Orton et al.*, 2010b].

3.3. Dissipation Estimates From ADV Data

[18] The inertial dissipation method (IDM) is a well-validated technique that has been used for decades to estimate the rate of dissipation of turbulent kinetic energy (ε) in a fluid flow [e.g., *Grant et al.*, 1962; *Voulgaris and Trowbridge*, 1998; *Zappa et al.*, 2003]:

$$\varepsilon = \Phi_i^{3/2} \kappa_i^{5/2} \alpha_i^{-3/2} \tag{2}$$

Here, dissipation is a function of angular wave number (κ_i) and the spatial power spectral density (Φ_i) of velocity over the "inertial subrange" of wave numbers, and index i refers to either the along-stream (i = 1), across-stream (i = 2), or vertical velocity (i = 3). The constant α_i is 0.51 if the along-stream velocity is used to compute Φ_i, whereas it is 0.68 if the across-stream or vertical velocity is used.

[19] Mean dissipation estimates were computed from spectra for 10 min periods of the ADV's axial velocity data, which typically exhibit the lowest noise levels [*Voulgaris and Trowbridge*, 1998]. Taylor's frozen turbulence hypothesis was utilized to convert from the measured temporal spectrum to the spatial spectrum Φ_i required above. Dissipation and 95% confidence intervals were computed using an approach we refer to as the Kolmogorov + noise (K+N) approach that subtracts off a white noise floor from the spectrum while computing dissipation [*Orton*, 2010]. This approach was particularly useful in this study, in which relatively noisy ADV data were collected using the highest velocity range setting on the instrument. Maximum wave numbers used to compute ε correspond to the smallest water motions that could be measured by each sensor without substantial bias due to spatial or temporal averaging. Given the ADV spatial averaging length scale of 0.009 m, the maximum wave number was 240 rad m^{-1}. Minimum wave numbers were chosen to be above the wave mode to avoid

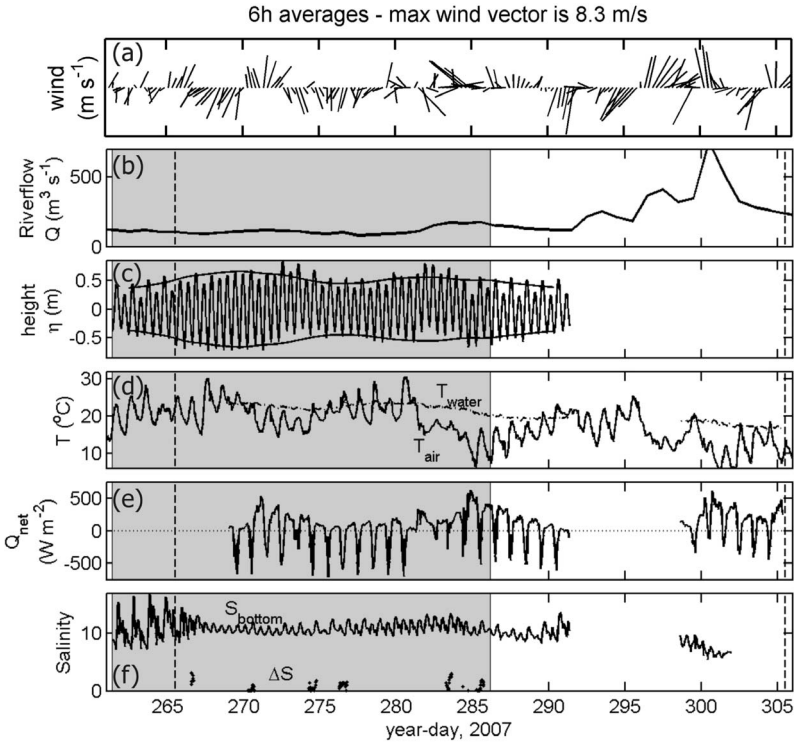

Figure 3. Time series of ambient conditions during the 2007 CASsIE study. The periods where various systems were deployed are indicated as ADCP deployment(shaded) and SOCa catamaran deployment (between dashed vertical lines). Variables include (a) wind velocity vectors for Piermont (pointing in direction wind is coming from), (b) river flow past Green Island Dam near Troy, New York, (c) observed water level (η), with the envelope of observed semidiurnal tidal range (from wavelet analysis) superimposed, (d) air (T_{air}) and water (T_{water}) temperatures, (e) estimated net upward surface heat flux, and (f) salinity measured on the ADCP tripod, at 30 cm above the bed (S_{bottom}), and the full water column vertical salinity difference (ΔS), from periods with CTD profiling.

wave bias in the dissipation estimate, which was determined from the pitch angular rate data measured by the vessel's inertial sensor.

[20] Strict quality control procedures were applied to omit periods that were not consistent with the K+N approach (a poor model-data fit), or wavy periods not consistent with Taylor's assumption. This included masking periods with estimated wave orbital velocities above 40% of mean velocity. Only 3% of the ε data were below 5×10^{-8} W kg^{-1}, but these were set to 5×10^{-8}, which is an estimate of the noise floor on the ADV dissipation measurement with this velocity range setting. While these data have high uncertainty, low values of dissipation are as important to keep as high values, to avoid biasing averages or regressions.

[21] ADV estimates of ε were compared with estimates from a pulse-coherent Doppler current profiler (a 2 MHz Nortek Aquadopp) on SOCa, for a spring flood tide with light winds (up to 3.2 m s^{-1}) similar to the periods used for compiling TKE budgets in this paper. The ADV relies on Taylor's frozen field assumption, but the Aquadopp measures the spatial velocity profile at 2.7 cm resolution (and 4 Hz), and does not require this assumption. Pulse-coherent Doppler profilers have been used previously to estimate near-surface ε in wavy conditions from a moving surface platform [*Gemmrich and Farmer*, 2004] and in the laboratory [*Veron and Melville*, 1999]. Dissipation computations for the Aquadopp used spectra for the along-stream velocities (an acoustic beam aimed forward at 50 cm depth from the front of SOCa), and were performed on each 1.02 m length profile, with spectra averaged over 10 min periods. The comparison showed moderate agreement over 2 orders of magnitude, from ~9×10^{-8} to 8×10^{-6} W kg^{-1}, but the Aquadopp estimates were a factor of 1.1–2.5 higher for the highest turbulence levels, and results were more scattered at low turbulence levels (Figure 4). Differences may arise due to the different range of wave numbers used for IDM with the two instruments, from 60 to 80 rad m^{-1} for the Aquadopp and from 80 to 250 rad m^{-1} for the ADV. Given the range of 2 orders of magnitude in the measured ε during the comparison, and other sources of uncertainty in dissipation measurements, the level of agreement of this comparison is encouraging and lends support to the ADV ε estimates during low winds during this study.

3.4. TKE Budget Terms From ADCP Data: P, B, T_D, ∂TKE/∂t

[22] Acoustic Doppler current profilers (ADCPs) are useful for measuring velocity of both the mean flow field and the larger turbulent motions over monthly or longer timescales. Janus configuration four-beam ADCPs sample

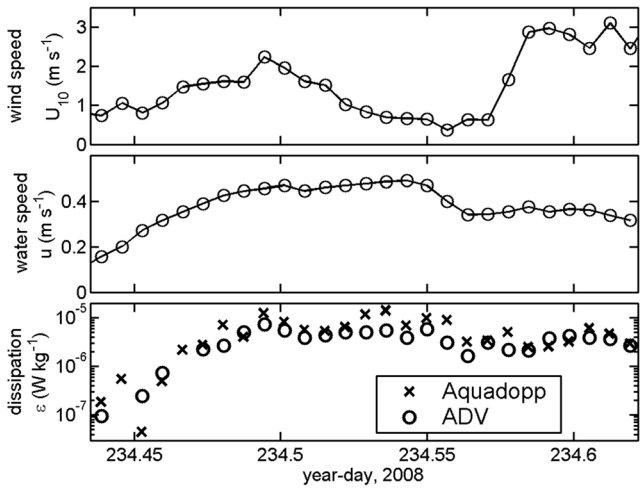

Figure 4. Observations during the ADV-Aquadopp dissipation comparison, including (top) wind speed, (middle) water speed, and (bottom) dissipation. Figure 4 (bottom) compares estimates of TKE dissipation at 50 cm depth using the two different sensors.

along-beam velocity (b_i) with two pairs of opposing beams angled at angle θ from vertical, where the subscript indicates a measurement at a numbered beam path (i = 1, 2, 3, 4). Accounting for the beam angles, beam velocities may be related to velocities in an orthogonal reference frame, u, v, and w, assuming that the velocities are homogeneous across the beam width.

[23] The four acoustic beams diverge to sample water parcels that are increasingly far apart with increasing distance from the transducer. The further this distance, the greater the spatial averaging of u, v, and w if the along-beam velocity data are transformed to an orthogonal velocity frame. This spatial averaging prevents accurate turbulence measurements, except in cases where the turbulent eddy scale is much larger than the spatial averaging scale. That is, in order to make an unbiased "direct computation" of Reynolds stress with ADCP orthogonal velocities, the flow velocities must be homogeneous across the distance between beams.

[24] The ADCP variance method avoids this bias, providing the vertical Reynolds stresses $-\overline{u'w'}$ and $-\overline{v'w'}$ directly from the beam angle and variances of the along-beam velocity data. This computation only assumes that the ADCP is perfectly level and motionless and the second statistical moments (e.g., $\overline{u'^2}$, $\overline{u'w'}$) are horizontally homogeneous between beams [*Stacey et al.*, 1999]:

$$-\overline{u'w'} = \frac{\left(\overline{b_2'^2} - \overline{b_1'^2}\right)}{4\sin\theta\cos\theta}, \quad -\overline{v'w'} = \frac{\left(\overline{b_4'^2} - \overline{b_3'^2}\right)}{4\sin\theta\cos\theta} \tag{3}$$

Kinetic energy in the mean flow is continually converted into small-scale turbulence, an energy flux measured by our ADCP as turbulent kinetic energy production (P). This is computed directly from these stresses and the mean shear:

$$P = -\overline{u'w'}\partial U/\partial z - \overline{v'w'}\partial V/\partial z \tag{4}$$

[25] For cases where waters are vertically stratified with differing densities, some TKE rearranges parcels of denser water above less dense water, increasing the potential energy of the water column. A method for estimating this buoyancy flux when P is available is to multiply P by the flux Richardson number, Ri_f, which is the ratio of buoyancy flux to shear production [*Peters*, 1999]:

$$B = -Ri_f P \tag{5}$$

A simple model for Ri_f presented by *Peters* [1999], as modified from *Schumann and Gerz* [1995], prescribes a range in Ri_f from 0 to 0.2 as a function of the gradient Richardson number. Considering that vertical profiles of density are not available for most periods, we simply assume an Ri_f of 0.2, a typical ceiling value for stratified waters [*Ivey and Imberger*, 1991]. The B term is typically at least a factor of 4 smaller than the P and ε terms [e.g., *Peters*, 1999], so uncertainty due to Ri_f is small relative to other sources of uncertainty in the TKE budgets.

[26] Along-beam velocity variances may also be used to observe TKE, first computing the quantity [*Lu et al.*, 2000; *Stacey et al.*, 1999]

$$Q = \frac{1}{4\sin^2\theta}\left(\overline{b_1'^2} + \overline{b_2'^2} + \overline{b_3'^2} + \overline{b_4'^2} - 4D\right) \tag{6}$$

Here, D is a bias due to Doppler noise. Doppler noise levels (D) are often assumed to be constant, but may have some variability due to the availability of waterborne particles for sound scattering [*Lu et al.*, 2000]. The TKE per unit mass is

$$\mathrm{TKE} = 0.5Q/\gamma, \text{ where } \gamma = \left(1 + 2\alpha\tan^{-2}\theta\right)/(1+\alpha) \tag{7}$$

Here, α is the anisotropy, $\overline{w'^2}/(\overline{u'^2} + \overline{v'^2})$, γ ranges from 1 to 2.7, corresponding to α from 0 to 0.5, from extremely anisotropic turbulence and isotropic turbulence, respectively [*Lu et al.*, 2000]. The TKE budget (equation (1)) contains the time variation of TKE, $\partial\mathrm{TKE}/\partial t$, computed by differencing successive 10 min averages of TKE.

[27] A technique for observing the turbulent vertical flux of TKE was recently developed and validated in the near-bed region of a bottom boundary layer by Stacey [*Stacey*, 2003], utilizing a sum of the third-order moments of along-beam velocity b_i:

$$K_3 = -\left(\overline{b_1'^3} + \overline{b_2'^3} + \overline{b_3'^3} + \overline{b_4'^3}\right) \tag{8}$$

This observed quantity contains information on the contribution of velocity along each beam axis to the flux, and accounting for the geometry of a Janus ADCP with 20° beam angles (default for a T-RDI ADCP), the vertical turbulent flux of TKE is [*Stacey*, 2003]

$$F_D = -\overline{w'\mathrm{TKE}} = \frac{1}{2}K_3\frac{1 + A_n}{0.6595 + 3.3191A_n} \tag{9}$$

This requires an estimate of an anisotropy factor defined as

$$A_n = \frac{\overline{w'^3}}{\left(\overline{w'u'^2} + \overline{w'v'^2}\right)} \tag{10}$$

This is the ratio of contributions to TKE vertical turbulent transport from vertical versus horizontal TKE and has been estimated to vary from 0.5 for isotropic bottom boundary layers to 1.5 for stratified, low-shear regions [*Stacey*, 2003].

[28] Finally, to return to the term of import to the TKE budget, the net turbulent transport, or vertical flux divergence of F_D is

$$T_D = \frac{\partial}{\partial z}\left(-\overline{w' \mathrm{TKE}}\right) = \frac{\partial}{\partial z} F_D \tag{11}$$

Single 10 min averages of T_D are noisy, so bin averaging of large quantities of data from similar phases of the tidal cycle is required [*Stacey*, 2003].

3.5. ADCP Turbulence Data Quality Control

[29] Potential sources of substantial bias in ADCP turbulence estimates include: instrument tilts, tilts with waves, and averaging in the vertical or temporal domain. An ADCP tilt of just 2° results in a bias of up to 17% in stress and shear production [*Lu and Lueck*, 1999]. Tilts for the CASsIE data set were ~0.6°, so tilt bias should be negligible. Avoidance of biases related to waves is of particular importance due to our interest in near-surface turbulence, especially given the large wind fetch at the CASsIE site in the Hudson. Wave filtration approaches have recently been presented, but generally risk biasing results because of additional assumptions on eddy scales or turbulence spectral shapes. In this paper, we focus on ADCP processing and the TKE budget for periods without waves (winds below 3 m s^{-1}), instead of taking on this additional complication. As an additional approach to avoid wave bias in turbulent quantities (beyond limiting our analyses to low-wind periods), we found it necessary to use the coherence between each acoustic beam's estimate of sea surface height (h_i) estimate and raw along-beam velocity (b_i) to omit entire profiles of turbulence data when near-surface bins have potential for wave bias [*Orton and Visbeck*, 2009].

[30] A comparison of low and high-resolution data sets is typically used to estimate the low bias in Reynolds stress due to temporal and spatial averaging during data collection [e.g., *Lu et al.*, 2000]. We determine correction factors for this bias by averaging neighboring beam velocity data in pairs (temporally or vertically) to create a new data set with half the sample density (the "low-resolution" data set), and compare the resulting turbulence estimates in linear regressions against those obtained with the full data set (the "high-resolution" data set) [e.g., *Orton and Visbeck*, 2009]. Using this approach, the spring tide deep channel ADCP resolution bias correction factor for τ_{xz} (or P) was 1.21, and for F_D (or T_D) was 1.13. The spring tide shallow shoal ADCP correction factors were 1.22 and 2.24, respectively, likely higher due to the shallower water and smaller turbulent length scales, as well as weaker turbulence.

3.6. Surface Heat Flux Estimates

[31] The net upward surface heat flux (Q_{net}) was estimated as a sum of latent, sensible, solar shortwave, and longwave fluxes. Solar absorption was assumed to occur within the water column, not at the bed, because minimum turbidity levels during calm wind and tide conditions with low river flow are typically 15–20 mg L^{-1} [e.g., *Orton and Kineke*, 2001] suggesting a minimum light extinction coefficient of ~1.5–2.0, so that 90% of light is typically attenuated in the upper 1–2 m [*Cloern*, 1987]. This is consistent with CASsIE observations during sunny, calm periods, when water temperature increases were mainly in the upper meter, and were negligible below 2 m [*Orton et al.*, 2010a]. The net longwave flux was estimated using the bulk formulae of *Clark et al.* [1974], which are shown to perform better in mid-latitudes than other parameterizations and have low mean bias when compared with extensive observations [*Josey et al.*, 1997]. Daily mean cloud cover was estimated from the solar radiation data [*Reed*, 1977]. Net water-to-air surface heat fluxes ranged from −710 to 620 W m^{-2} (Figure 3), with specific components of the flux having the following ranges: solar −814 to 0 W m^{-2}, latent −40 to 370 W m^{-2}, longwave 5 to 189 W m^{-2}, and sensible −50 to 140 W m^{-2}.

[32] The solar shortwave flux was measured, but the other budget terms were estimated using measured variables in bulk formulae, so it is useful to examine an overnight heat budget to evaluate their accuracy. A useful period for this test is from year day 284.75 to 285.22, a period with strong heat loss when mean water column salinity change and velocity were near zero, suggesting that effects of advection on the budget should be negligible. Discrete CTD profiles show that the water column was well mixed at the start and end of the period, so it is reasonable to use a full water column heat budget. The estimated Q_{net} was 504 W m^{-2}, and a simple heat budget suggests that this was accurate: the measured depth-averaged water column temperature decrease was 0.91°C, and if it is assumed that the air-water heat flux is the dominant controlling factor, this requires an average 463 W m^{-2} heat flux, 9% below the estimated value.

[33] In spite of using bulk flux estimates of heat and momentum (wind stress), our approach utilizing in situ measurements from SOCa constitutes a significant improvement beyond many prior studies. Observational studies often use remotely measured wind, humidity and temperature to compute air-water fluxes and wind stress (e.g., at an airport or offshore buoy), and this can lead to large errors due to strong spatial variability in coastal regions [*Orton et al.*, 2010a]. Future studies should improve on our approach with either direct eddy covariance or atmospheric profile based flux estimates [*McGillis et al.*, 2001], the latter method of which has been used on subsequent deployments of the catamaran. Longwave radiation measurements are also possible with off-the-shelf products.

3.7. Additional Derived Quantities

[34] A continuous wavelet transform (CWT) was used to quantify tidal forcing, decomposing observed water level data measured by the CTD on the ADCP tripod into semi-diurnal (D2) and diurnal (D1) species. This provides D2 tidal ranges (Figure 3) and also the D2 tidal current phase that is utilized below for tidal phase bin-averaged data presentations. The fundamental benefit of the CWT over traditional harmonic analysis is that it resolves the time variation of frequency content, with no assumption of stationarity [*Jay and Flinchem*, 1999].

[35] Bed stress (τ_{b},) was computed using linear extrapolations to the bed of the bottom five stress measurements in the water column [*Orton and Visbeck*, 2009], and the

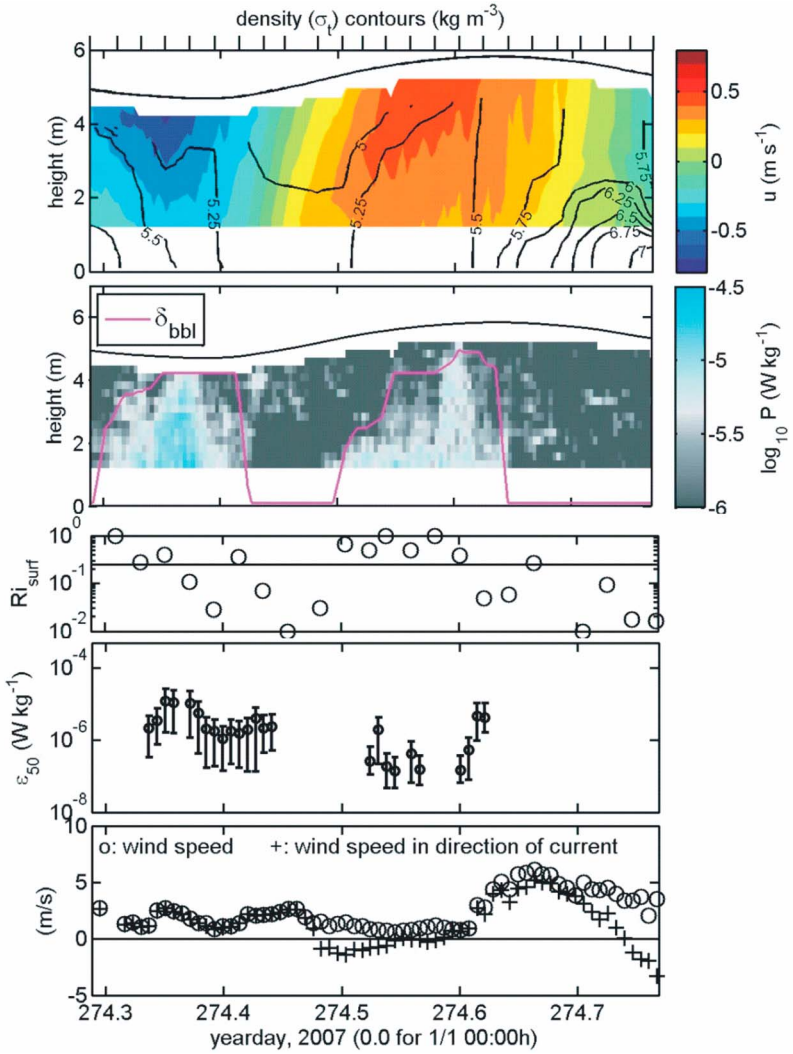

Figure 5. Water and wind conditions during one 12 h time series, 4 days after a strong spring tide. Shown are along-stream velocity (u), contours of water density anomaly (σ_t), TKE shear production (P), bottom boundary layer height (δ_{bbl}), near-surface Richardson number (Ri_{surf}), TKE dissipation (ε) at 50 cm depth, wind speed, and wind speed in the direction of the water current. Times of CTD profiles are shown with external x axis ticks in the first panel.

bottom shear velocity is $u_* = \sqrt{\tau_b/\rho}$, where ρ is water density. The water-side shear velocity (U_*) due to wind was computed using this equation with the bulk estimates of wind stress. For time series of u_*, this often led to undefined values on neaps or near slack tides because stress estimates were noisy and near zero. To produce a more continuous data set for use in regressions or turbulent buoyancy flux computations, a drag coefficient of 0.0014 was used with the near bed velocity (1.25 m height) and a quadratic drag law to compute u_*, giving good agreement with the regression estimates of u_*.

[36] The gradient Richardson number (Ri) is a nondimensional number useful for diagnosing the dynamic stability of the water column, with values below 0.25 typically indicating potential for instability [*Geyer and Smith*, 1987]. Ri was computed using the observed squared buoyancy frequency ($N^2 = g/\rho_0 \partial\rho/\partial x$) from 25 cm bins of CTD data, divided by 30 s averages of mean squared shear. We define the bottom boundary layer (δ_{bbl}) as the continuously turbulent range of heights above the bed, capped by either (1) a zero intercept (stress) in a regression of near bed stress versus height or (2) the first height where turbulent stress is not detected [*Orton and Visbeck*, 2009].

4. Results

[37] Fortnightly variability typically expected for a partially mixed estuary was observed at the 5 m deep shoal site in the time series and 12 h anchor station data. The fortnightly tidal cycle had a strong impact on near-bed salinity (Figure 3) and stratification, with peak stratification of 4 and 0.8 kg m^{-4} on weak neap and strong spring tides, respectively. Most tidal cycles exhibited periodic stratification (e.g., Figure 5), with the duration of well-mixed conditions (if any) typically depending on the strength of the tide.

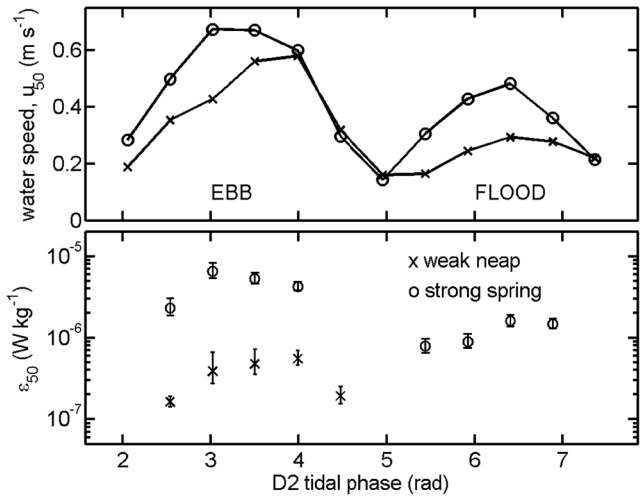

Figure 6. Tidal phase bin-averaged (top) water velocity and (bottom) dissipation, for periods with low winds ($U_{1.2}$ below 3 m s^{-1}). The legend designates neaps (year days 275–280 and 304–306) and strong spring tides (year days 298–300). Error bars show the 95% confidence intervals on the mean, assuming a lognormal distribution.

[38] Semidiurnal phase relationships of stratification and velocity were typically similar to those expected for a lateral shoal [*Scully et al.*, 2009], with substantial differences relative to typical deep channel circulation patterns. One example of a 12 h tidal cycle anchor station data set that was collected 4 days past a strong spring tide is shown in Figure 5. The strongest pulse of saline water and stratification typically arrived late in flood tide, likely due to bottom Ekman forcing causing cross-channel impingement of the salt wedge onto the shallow west side of the estuary [*Scully et al.*, 2009].

[39] There were also signs of strong atmospheric effects on water column stratification during the CASsIE study at the shoal site. Temperature was frequently an important contributor to the full water column vertical density gradient, with temperature contributing 30% or more to the gradient in 25% of the time series profiles at the shoal site, predominantly in the warm weather period early in the study. A 12 h CTD time series on year day 276 showed the effects of solar heating on a sunny afternoon with calm winds, with temperature enhancing upper water column stratification (from 0.5 to 1.5 m depth) by 50–100%, relative to salinity stratification alone [*Orton et al.*, 2010a]. Fall season storms were also observed by SOCa, with mean along-estuary winds as high as 11.0 m s^{-1} (1.2 m height) gusting as high as 19 m s^{-1} (e.g., year days 273.5–275.0 and 299.8–300.2), and were typically followed by periods of reduced stratification.

[40] The deep channel site typically exhibits stronger stratification, with minima and maxima about 3 days past neap and spring tides, respectively. For along-channel water density transects typical of spring and neap conditions, as well as a complete climatology of stratification in the estuary, the reader is referred to *Orton and Visbeck* [2009]. The two along-channel CTD transects are not presented here, but showed that the large-scale along-estuary density gradient ($\partial\rho/\partial x$) measured from stations to the north and south of the study site (Figure 2) were -7.6×10^{-5} kg m^{-4} on 13 September 2007 and -9.8×10^{-5} kg m^{-4} on 1 November 2007.

[41] Ebb tides during CASsIE had stronger near-surface currents and turbulence than floods, regardless of fortnightly tidal phase (Figure 6). TKE shear production for the period shown in Figure 5 was as high as 3×10^{-5} W kg^{-1}, but the ADCP only detected shear production in the upper half of the water column near peak flood and ebb. Surface-based SOCa estimates of TKE dissipation data at 50 cm depth during this period varied from $\sim 1 \times 10^{-7}$ to 7×10^{-4} W kg^{-1}. Net turbulent transport is not shown because it requires additional averaging, but is presented below in section 4.2, along with broader comparisons of P, ∂TKE/∂t and ε_{50}.

[42] Levels of near-surface TKE dissipation (ε_{50}) are potentially related to several different variables, including winds, proximity or outcropping of the bottom boundary layer, near-surface TKE shear production, water speed or gradient Richardson number. The highest ε_{50} estimates of 2×10^{-5} W kg^{-1} in Figure 5 were during ebb tide, at year day 274.36. This period exhibited the tidal cycle's maximal near-surface water speed (50 cm s^{-1}) and shear production ($\sim 10^{-5}$ W kg^{-1}), as well as 3 m s^{-1} winds, and BBL turbulence extending from the bed to near the sea surface. Flood tide had relatively low ε_{50} values until year day 274.62, when it rapidly increased, again coincident with increases in many of the same variables. Below, we attempt to determine relationships between these variables and ε_{50} by using regression analyses, quantifying the TKE budget, and examining possible dynamical explanations.

4.1. Near-Surface Dissipation Observations and Regressions

[43] Wind speed clearly had a strong influence on ε_{50} during the study (Figure 7), and a log-log least squares regression using U_*^3 shows significant correlation ($\alpha < 0.001$) and can account for 41% of the variance in ε_{50} (Table 1). However, the wall layer model in Figure 7 ($\varepsilon = U_*^3/\kappa z$) underestimated ε_{50} for most cases. Mean drag coefficients for wind-blown seas are typically below 0.002 for winds below 15 m s^{-1} [*Drennan et al.*, 2005], yet it would require a geometric mean drag coefficient of ~0.005 to fit the bulk of the data. This suggests that additional processes beyond simple wind-generated shear instabilities were leading to higher turbulence levels. Note that a conservative approach is used to assess the significance of correlations using the effective degrees of freedom, the number of independent "events" that contribute to the correlation, defined as edof = N/N_{ccv}, where N_{ccv} is the number of lags over which the cross-covariance function rolls off by 50%.

[44] Tidal currents and bottom boundary layer growth to the water surface appear to only have had a weak influence on ε_{50}. Evaluating the bottom wall layer dissipation scaling of $\varepsilon_{50} \sim u_*^3$, the log of u_*^3 could explain only 10% of the variance in the log of ε_{50}. In cases where δ_{bbl} approached the sea surface, the median increase in dissipation over the 30 min before to after the time of reaching the surface was a factor of 2.00, though in a few cases it was an order of magnitude.

[45] Variables related to turbulence generation by shear instability showed weak-to-moderate correlations with dissipation. A linear least squares regression using surface water

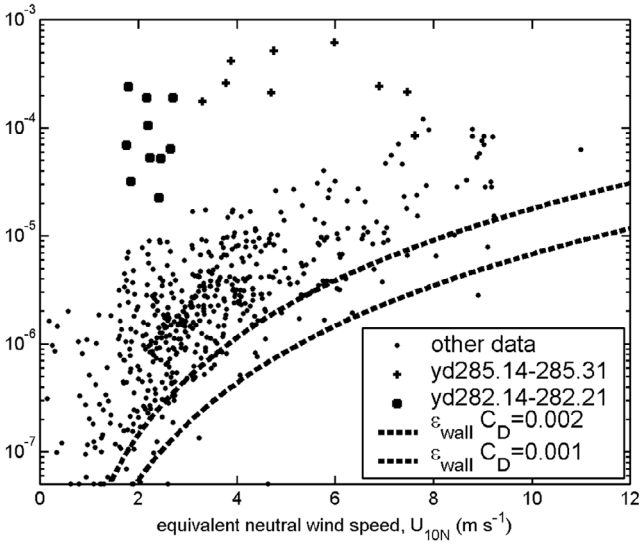

Figure 7. The relationship between wind speed and dissipation (50 cm depth), measured on SOCa. Dashed lines show the uncertainty range for the wall layer model for wind-generated turbulence within a range of ±33% of an estimated quadratic drag coefficient of 0.0015. The squares and pluses are from two weak spring ebb tides that exhibited anomalously high dissipation, the squares with strong shear and currents (section 5.3) and the pluses with strong heat fluxes and no stratification (section 5.5).

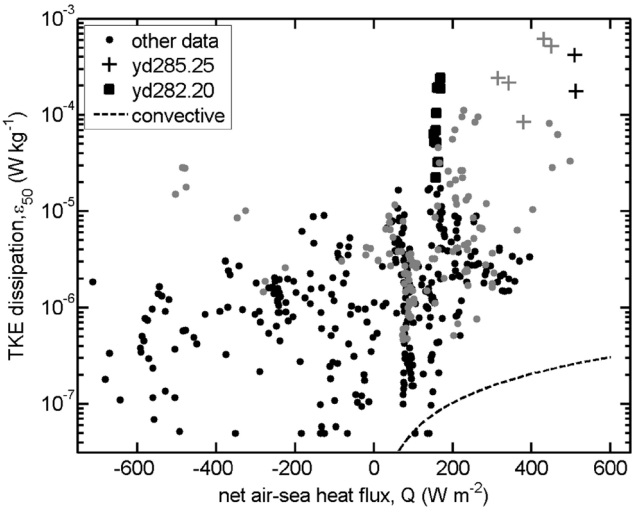

Figure 8. The net air-sea heat flux (Q_{net}) and dissipation have a moderate positive relationship for low winds or all data. Points in black have wind speeds ($U_{1.2}$) below 3 m s^{-1}, while gray points have stronger winds. The dashed line shows the maximum ε that could result from free convection caused by surface cooling (i.e., 100% of the buoyancy loss is converted to TKE). However, Q_{net} could also influence turbulence by promoting or destroying stratification, impacting the potential for shear instability. Squares and pluses are as in Figure 7.

speed shows significant correlation with $\log_{10}\varepsilon_{50}$ ($r^2 = 0.30$; $\alpha = 0.02$) when using cases where wind speed was below 3 m s^{-1} (Table 1). A significant correlation is also present between surface water speed and $\log_{10}\varepsilon_{50}$ when using all data ($r^2 = 0.14$; $\alpha = 0.01$). While there was no correlation for surface water shear, the negative correlation for the log of near-surface gradient Richardson number (Ri_{surf}) was low-to-moderate ($r^2 = 0.18$). Ri_{surf} data were only available for the anchor station time series, so were fewer in number than any other variable used in the regression analysis ($N = 78$), resulting in very low edof (8) and marginal significance ($\alpha = 0.30$) in spite of the correlation (Table 1).

[46] Variables related to air-sea heat fluxes had moderate correlations with dissipation, suggesting possible causative relationships (e.g., Figure 8). There was a significant positive correlation ($r^2 = 0.17$, $\alpha = 0.06$) between the net air-sea heat flux (Q_{net}) and $\log_{10}\varepsilon_{50}$. There is a slightly stronger positive correlation ($r^2 = 0.22$) for periods of heat loss from water to atmosphere ($Q_{net} > 0$), and no correlation during periods with heat gain into the water such as sunny and/or hot, windy afternoons ($Q_{net} < 0$).

4.2. Near-Surface TKE Budgets

[47] Near-surface TKE budgets are examined here, focusing on low-wind spring tide cases where length scales are relatively large and the signal-to-noise ratio is relatively good. Spring ebbs in the Hudson have been shown to have the strongest TKE dissipation [*Peters*, 1999], and account for a large percentage of the vertical salt flux over fortnightly spring-neap tidal periods [*Nepf and Geyer*, 1996]. Profiles of velocity, turbulence length scales, and TKE budget terms are shown in Figures 9–11, for the shoal and channel sites. A contrast is typically evident between ebb and

Table 1. Results of the Correlation Analysis for $\log_{10}\varepsilon_{50}$

Independent Variable	Variable Name	r^2	N	edof[a]	α[b]	Details
$\log_{10}U_*^3$	surface turbulence scale	0.41	538	54	<0.001[c]	for all data
Q_{net}	sea-to-air heat flux	0.17	432	22	0.06[c]	for all data
$\log_{10}u_*^3$	bed turbulence scale	0.10	247	24	0.14	for all data
u_{surf}	water speed	0.14	506	50	0.01[c]	for all data
u_{surf}	water speed	0.30	180	18	0.02[c]	$U_{1.2} <= 3$ m s^{-1}
u_{surf}	water speed	0.02	342	34	>0.33	$2 < U_{1.2} <= 5$
u_{surf}	water speed	0.03	50	5	>0.33	$5 < U_{1.2}$
$\log_{10}Ri_{surf}$	Richardson number	0.18	78	8	0.30	for all data
du_{surf}/dz	surface shear	0.00	380	38	-	for all data

[a]Effective degrees of freedom, edof = N/N_{ccv}, where N_{ccv} is the cross-covariance roll-off scale.
[b]Significance test, α is the probability of a type I error, false correlation by random chance.
[c]Significant results ($\alpha \leq 0.10$).

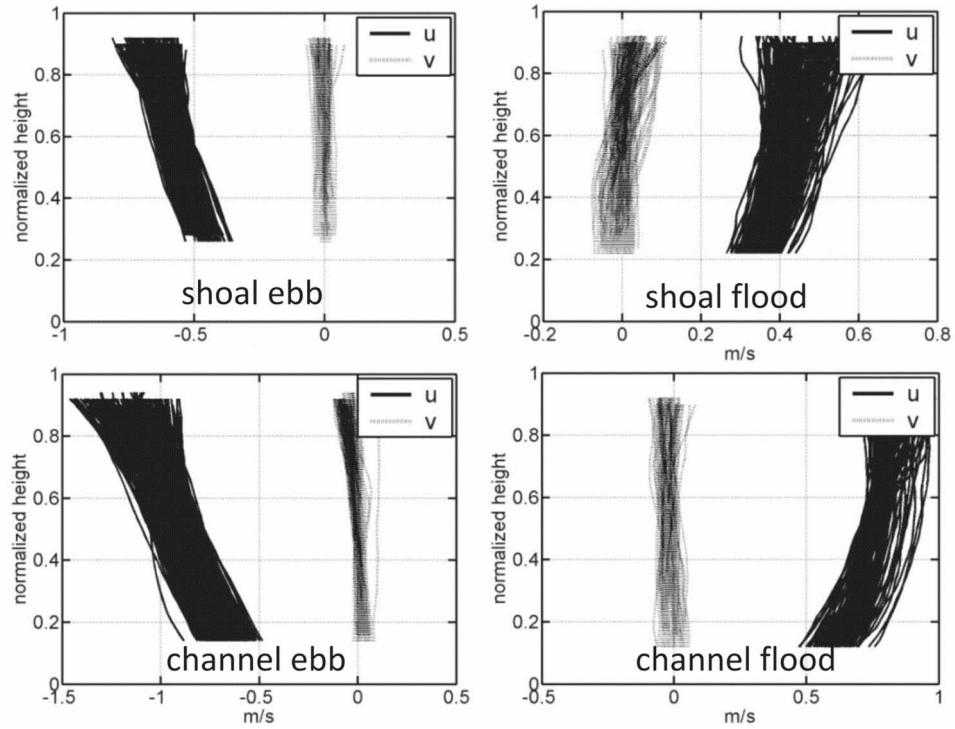

Figure 9. Velocity profiles for periods used in the strong spring tide TKE budgets (Figure 11). The 60–100 ten minute average profiles are all superimposed to show the typical velocity structure. Mean water column depths are (shoal) 5.1 m and (channel) 15 m.

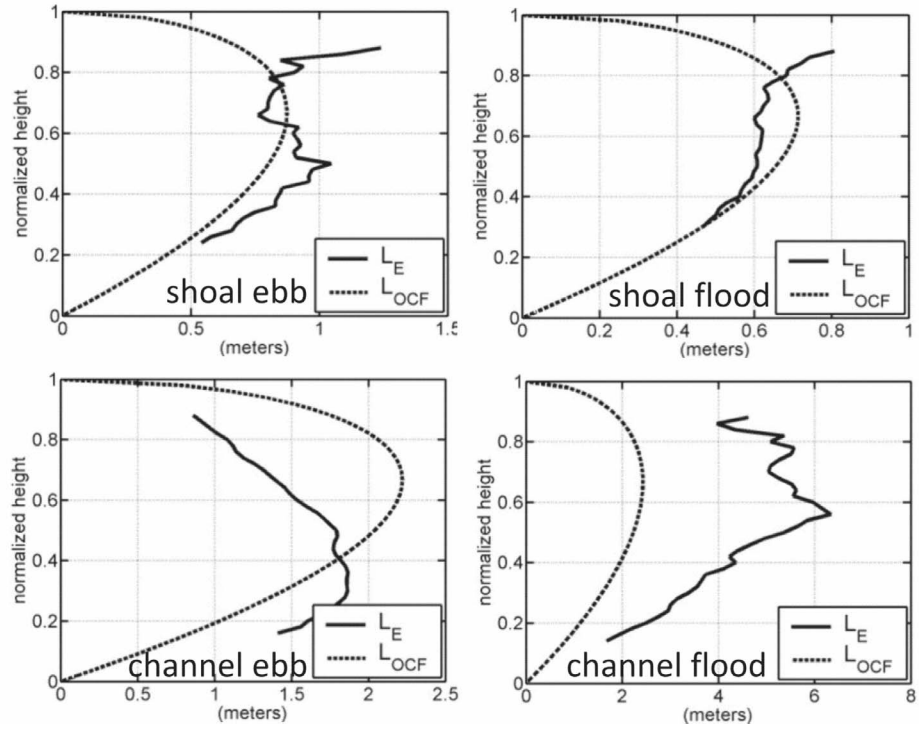

Figure 10. Vertical turbulence length scales for the periods used in the strong spring tide TKE budgets (Figure 11). Shown are mean profiles of the estimated Ellison turbulence length scale (L_E) and the theoretical open-channel flow limit due to the bed and sea surface boundaries (L_{OCF}).

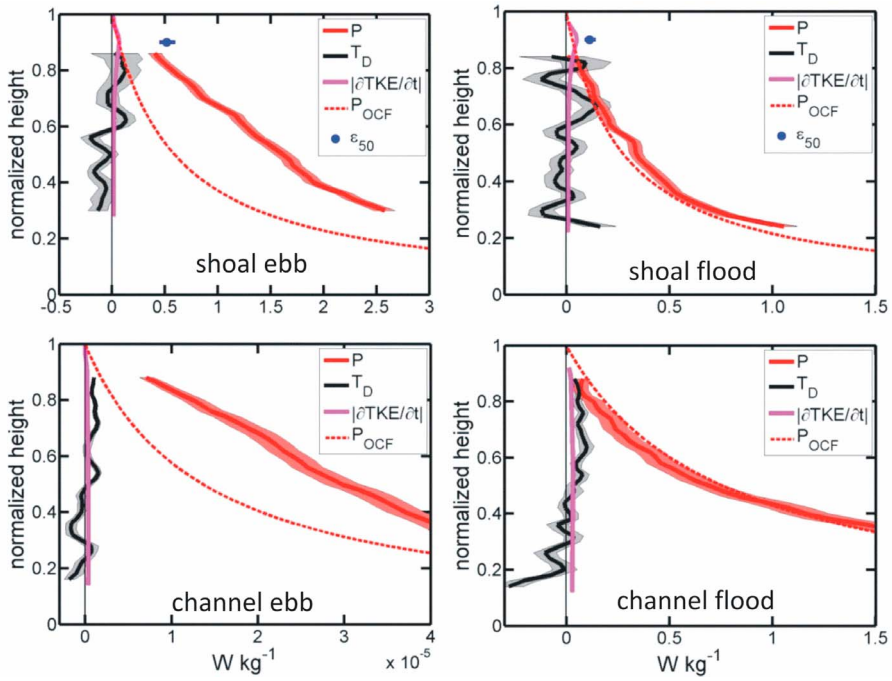

Figure 11. Mean TKE budget terms for strong spring tides with low winds: TKE shear production (P), net turbulent TKE flux (T_D), mean absolute value of TKE tendency (∂TKE/∂t), and dissipation at 50 cm depth (ε_{50}) from SOCa (shoal budget only). Observed standard error is shown as shading around T_D and P and as a horizontal line for ε_{50}. For the shoal site, the near-surface TKE budget is quantified at ~50 cm depth as $\partial\text{TKE}/\partial t = P - 0.2P - \varepsilon + T_D$ (section 4.2). An open-channel flow model of P is also shown for comparison (P_{OCF}).

flood tides, with shear throughout the water column on ebbs and weak upper water column shear on floods (Figure 9), though this is more consistently the case for the deep channel site. The shoal site budgets utilize additional data from 2006 at the same site, using the same ADCP settings, to improve the signal-to-noise ratio. Consistent with predictions of *Stacey* [2003], a large number of profiles must be averaged to reduce observational uncertainty for T_D. The average length scales and TKE parameters presented here are averages of 60–100 ten minute average profiles, so 3600–6000 ensemble averages of velocity (each an average of over 10 individual "subping" measurements).

[48] An analysis of theoretical turbulence length scales in comparison to vertical averaging length scale suggests that the turbulence was well resolved. A theoretical vertical length scale for the turbulence expected to dominate energetically is the Ellison scale, which has been shown to be triple the Prandtl scale of $L_m = \overline{u'w'}^{0.5}\ (\partial\overline{u}/\partial z)^{-1}$ [*Stacey et al.*, 1999]. However, the open-channel flow length scale imposed by the proximity of the seabed and surface, $L_{\text{OCF}} = \kappa z\ (1 - z/h)^{0.5}$ [*Scully et al.*, 2010; *Simpson et al.*, 1996], would limit the scales as shown in Figure 10. Length scales during spring tides were well above the vertical cell size of 25 cm, though only by a factor of 2–3 during shoal spring floods. The effective vertical averaging during sampling is similar to a triangular filter of data and covers as much as two times the cell size (50% overlap). However, only ~16% of the weighting comes from outside the depth cell [*Pulkkinen*, 1993], so the depth cell size is a good estimate of the ADCP vertical averaging length scale.

[49] The shoal TKE budget for strong spring ebbs (Figure 11, top left) is closed to within their uncertainty levels, with a close similarity between ε_{50} (5.2×10^{-6} W kg^{-1}) and P at 60 cm depth (4.2×10^{-6}). Ebb P was well above a bed-driven wall layer model ($P_{\text{wall}} = u_*^3/\kappa z$) or an open channel flow model, $P_{\text{OCF}} = u_*^3(1 - z/h)/\kappa z$ [e.g., *Voulgaris and Trowbridge*, 1998]. Flood tide ε_{50} and near-surface P were much smaller (10^{-6} W kg^{-1} or lower). Flood P was similar to values predicted by the open channel flow model throughout the water column, but signal-to-noise levels for shoal floods were too low to quantify the near-surface TKE budget. These are low-wind periods (below 3 m s^{-1}), and wind-driven shear production at 50 cm depth should be relatively low, because for 3 m s^{-1} winds (the maximum here) the wind-driven wall layer modeled production is 3×10^{-7} W kg^{-1}.

[50] The deep channel TKE budget terms (Figure 11) similarly show flood turbulence follows the open-channel flow model, and ebb turbulence is well above the model prediction. On flood, T_D approaches the magnitude of P in the upper water column, but both are substantially lower than the ebb P values.

[51] Turbulent TKE transport (T_D) was a noisy measurement, in spite of the extensive temporal averaging. When T_D was significantly different from zero, it was qualitatively consistent with a Fickian diffusive transport model for an unstratified boundary layer flow [*Scully et al.*, 2010], where the near-bed region of high TKE exports it vertically to the region of low TKE in the outer part of the boundary layer: T_D values near the bed were negative (a loss of TKE) and in the upper water column were positive (a gain of TKE).

ADCP estimation of T_D was limited to spring tides and generally not possible for periods with weaker turbulence.

[52] The mean of the absolute value of the TKE tendency term, $|\partial \mathrm{TKE}/\partial t|$, is plotted in Figure 11 and was typically well below 10^{-6} W kg^{-1}. TKE measurements with equation (7) require subtraction of the noise floor (D) in equation (6), but $\partial \mathrm{TKE}/\partial t$ should not be sensitive to this correction because time dependence of D is low: prior studies have found that D at a given height above the bed was relatively constant with time [*Lu et al.*, 2000; *Stacey et al.*, 1999].

5. Discussion

[53] Here, we compare our results to a prior study of TKE dissipation in the Hudson, then assess the dominant drivers of near-surface dissipation in the Hudson, reflecting in general on characteristics of partially mixed or salt wedge estuaries. Wind stress generation of turbulence clearly is dominant, but we also examine the relative importance of bed stress versus shear instability, the roles of ebb and flood tidal dynamics, and impacts on water column stratification of buoyancy fluxes due to tidal straining, turbulent mixing, and surface heat fluxes.

[54] Several days of measurements of turbulence from near the bed to the upper water column along the deep channel of the lower Hudson (alongside Manhattan) showed the importance of stratification and local shear instability outside the bed log layer [*Peters*, 1999; *Peters and Bokhorst*, 2000]. They observed strong turbulence in the bottom boundary layer, weak turbulence in and above the pycnocline during neap tides, and low Ri and high ε through the water column during spring ebbs. Turbulence in the stratified water column well above the bottom appeared to be locally generated by shear instability, and was 10^{-5} W kg^{-1} on spring ebbs, well above levels predicted by the wall layer dissipation model. That study did not include measurements above ~2.5 m depth, or address wind generation, or include overnight observations, so our study provides a unique data set for addressing some of the same but also some different processes.

5.1. Wind Stress Generation of Turbulence

[55] It is well established that winds can influence upper ocean turbulence, though studies of direct wind generation of turbulence in estuaries are somewhat rare. Turbulence can be generated directly through shear (e.g., wall layer model), through wave breaking [*Gemmrich and Farmer*, 2004], and through interactions of shear and waves such as Langmuir cells [e.g., *Gargett and Wells*, 2007]. It has also been shown that along-channel winds can modify stratification and indirectly strengthen or weaken turbulence through wind straining [*Chen and Sanford*, 2009; *Scully et al.*, 2005].

[56] The study was conducted at a broad, straight section of the Hudson and thus wind is expected to have a strong influence on near-surface turbulence, particularly for along-channel winds. The cross-channel fetch is ~1.8 km in each direction, and the along-channel fetch is over 14 km to the north and much longer to the south. There is a significant correlation between the wind-driven shear velocity cubed (U_*^3) and ε_{50} in the CASsIE study (Table 1). This study does not examine details of the role of wave breaking, but rather focuses on periods with low-to-moderate winds where multiple processes may be important.

[57] The fact that ε_{50} was above the wind-driven wall layer model can result from a number of processes superimposed on wind-driven shear, including those listed above. At wind speeds (U_{10N}) above ~5 m s^{-1}, wind wave breaking was typically observed, and likely explains ε_{50} above the wall layer model. At wind speeds below 5 m s^{-1}, dissipation above the wall layer prediction may result from superimposition of tide- and wind-driven currents; as described in section 3.3, periods with weak currents were masked to avoid ε_{50} biases due to waves and Taylor's assumption. The good agreement between the spatial Aquadopp measurement and the temporal ADV estimates of ε_{50} for similarly low winds (section 3.3) suggests that waves, vessel motion, and the use of Taylor's assumption were not causing biases for winds below 3.2 m s^{-1}.

5.2. Ebb Dominance of Near-Surface Dissipation

[58] Near-surface turbulence was typically stronger on ebb tides than floods, at both the shoal and channel sites (Figures 6 and 11). Spring flood tides had moderate currents but still had a low ε_{50} average, below 2×10^{-6} W kg^{-1} (Figure 6). Multiple processes exist that could cause differences in ε_{50} for flood versus ebb tides. One possible reason for stronger ebb turbulence is obvious from Figure 5: stronger tidal currents and shallower water depth lead to stronger shear. In shallow estuaries with a progressive tidal wave, the peak ebb velocity is near the time of minimum depth, and the peak flood near the time of maximum depth. For a given tidal volume transport, depth-averaged shear is weaker on flood tides.

[59] The weaker ε_{50} and P on flood versus ebb tides can also be attributed to the dynamics of a partially stratified estuary. On ebbs, due to the opposition of barotropic (down estuary and constant with depth) and baroclinic (up estuary, maximal at the bed) pressure gradient forces, as well as due to differential advection of the along-channel salinity gradient (tidal straining), the entire water column has shear [*Stacey and Ralston*, 2005]. This pattern is observed for the spring tide periods, and particularly for the deep channel site: there is strong upper water column shear on ebbs (Figure 9) and strong shear production leads to relatively high ε_{50} (Figure 11). Alternatively, on flood tides, the alignment of these forces and the negative tidal straining buoyancy flux lead to a well-defined bottom boundary layer and pycnocline with maximum velocity (and zero shear) at the top [*Stacey and Ralston*, 2005]. In this case, since shear instability must be zero at this location, and shear is relatively weak above, near-surface ε_{50} is low. Also, T_D in the flood bottom boundary layer was typically observed to be toward the pycnocline from below, and weak above the pycnocline, similar to the initial observations using the ADCP third moments method for observing T_D [*Stacey*, 2003]. During strong spring flood tides, the bottom boundary layer can reach the sea surface, but at the sites observed in this study, the resulting near-surface turbulence is much weaker than during spring ebbs (Figure 11).

5.3. Role of Bed Stress Versus Local Shear Instability

[60] A major goal of the research project was to study how strong tidal currents and a turbulent bottom boundary layer

could cause strong near-surface turbulence. However, u_* (or bed stress) had only a weak correlation with ε_{50}, and there was only a median ε_{50} increase of 2.00 when the bottom boundary layer reached the sea surface (section 4.1). Net turbulent transport of TKE (T_D) approached the same magnitude as P in the upper water column on flood tides at the channel station (Figure 11) but dropped toward the upper few meters. However, the magnitude was small relative to spring ebb P, and this likely points to the difference between rough bed, unstratified waterways where T_D is important [*Hurther et al.*, 2007] and relatively smooth bed, frequently stratified estuaries such as the Hudson.

[61] Due to the complex role of stratification, a simple parameterization for near-surface turbulence and air-sea fluxes utilizing bed stress with wall layer scaling [e.g., *Chu and Jirka*, 2003] or an open-channel flow model will often be inaccurate for a partially stratified (or salt wedge) estuary. Stratification can have complex effects due to its impact of damping turbulence but also accompanying and promoting enhanced shear on ebb tides, leading to local shear instability high in the water column (see section 5.2). Moreover, it is possible that increases in suspended mud during periods with high bed stress provide a negative feedback on turbulence, causing sediment-induced stratification and raising *Ri*, as can occur in the Hudson's turbidity maximum off Manhattan [*Orton and Kineke*, 2001].

[62] Shear instability is typically the dominant turbulence generation mechanism in estuaries [*Geyer and Smith*, 1987; *Peters and Bokhorst*, 2000], whether near the bed or far from it. However, local shear instability in regions with strong shear high in the water column can produce strong turbulence near the surface. Surface water speed showed some correlation with ε_{50}, but mainly only at water speeds above 50 cm s^{-1}. For a given water speed on a neap tide, the dissipation is much lower than for the same water speed on a spring tide (Figure 6). This is likely because in partially stratified estuaries, outside of well-mixed flood tide bottom boundary layers, shear often accompanies stratification and the gradient Richardson number (*Ri*) is often near the critical value for shear instability, 0.25 [e.g., *Chant et al.*, 2007]. The regression of Ri_{surf} and dissipation had moderate correlation ($r^2 = 0.18$) but too few independent events to be statistically significant (Table 1). While the variables should be related, a low *Ri* also does not necessarily require there to be substantial TKE and dissipation, so the lack of a stronger correlation is not surprising.

[63] High values of ε_{50} from year day 282.14–282.21 (Figures 7 and 8) appear to have been related to small-scale shear instability in the upper water column, as the ADCP shows strong shear and water speeds from 70 to 80 cm s^{-1}. However, ADCP estimates of P and the Ellison turbulent length scale were near zero during this period, likely due to turbulence length scales being smaller than the ADCP vertical averaging length scale of 25 cm. No CTD profile data were collected at this time, but observations during an ebb tide on the following day showed strong stratification (up to 2.5 kg m^{-4}). The Ozmidov scale is a theoretical length scale for the largest eddy that can occur in a stratified flow, $L_O = \varepsilon^{0.5} N^{-3/2}$, and equals 0.14 m for this stratification and logarithmic mean ε_{50} of 7.8×10^{-5} W kg^{-1}, so it is reasonable that the ADCP would not detect this episode.

5.4. Buoyancy Flux Impacts on Upper Water Column Stratification

[64] Processes that govern water column stratification can indirectly impact turbulence generation, and are typically examined in terms of depth-integrated buoyancy fluxes in W kg^{-1} [*Stacey et al.*, 2001; *Stacey and Ralston*, 2005] or the temporal change of the vertical potential energy anomaly in W m^{-3} [*Simpson et al.*, 1990]. Here, we estimate and compare buoyancy fluxes due to wind- and tide-driven turbulent vertical mixing, spatial transport (tidal straining), and the surface heat flux, seeking dynamical clues to view alongside our observed correlations and budgeting results. Similar results are found when comparing contributions of each term to the vertical potential energy anomaly. Wind straining [e.g., *Scully et al.*, 2005] is not considered: the Wedderburn number had almost no correlation with ε_{50}, likely because wind-driven mixing increases in importance as you near the sea surface.

[65] The estimated surface net heat flux (Q_{net}) provides a water column buoyancy flux in the upper layer, using the convention here of positive flux for a gain in water buoyancy [*Imberger*, 1985]:

$$B_{surface} = -Q_{net}\alpha g / c_p \rho \tag{12}$$

Here, we have incorporated the heat capacity (c_p) and thermal expansion coefficient (α) for water.

[66] Turbulent buoyancy fluxes due to both tide-driven ($B_{turb,tide}$) and wind-driven ($B_{turb,wind}$) turbulent mixing were approximated using the negative of wall layer scaling of P and the flux Richardson number (equation (5)). The total turbulent buoyancy flux from wind and tides could alternately be estimated using observed shear production levels, but wavy periods have been omitted from the ADCP turbulence data set, so this makes it impossible to quantify mixing for all periods. A rough estimate of upper water column buoyancy destruction due to wind-driven turbulent mixing at 1 m depth was made using the wall layer scaling. The along-channel buoyancy flux due to tidal straining on the shoal was approximated using the scaling of *Stacey and Ralston* [2005], $B_{shear} = g/\rho_0 \, (\partial\rho/\partial x) \, \Delta u \, \delta_{bbl}$, with a constant $\partial\rho/\partial x \approx 1 \times 10^{-4}$ kg m^{-4} based on the observed values (section 4). Here, the velocity difference scale used for shear is $\Delta u = 2u_*/\kappa$, a scale for the difference between the mean bottom boundary layer speed and the water speed just above the top of the layer.

[67] Resulting time series of each buoyancy flux are shown with upper water column stratification data in Figure 12. During sunny periods with weak winds (e.g., Figure 12, left), buoyancy fluxes due to tidal processes and surface fluxes are of similar order. During a stormy period (Figure 12, right), the wind mixing term was dominant through much of the period, but the study's strongest surface cooling and surface buoyancy flux were observed overnight as the storm ended. In spite of similar tidal straining and turbulent buoyancy fluxes, the ebb on the sunny day (276) restratified the upper water column, whereas the ebb on the cold morning (285) did not, suggesting the large difference in surface heat flux was an important factor. A cross-channel transect on year day 285 showed that the stormy period did not cause total estuarine destratification, so this was only a local shoal destratification

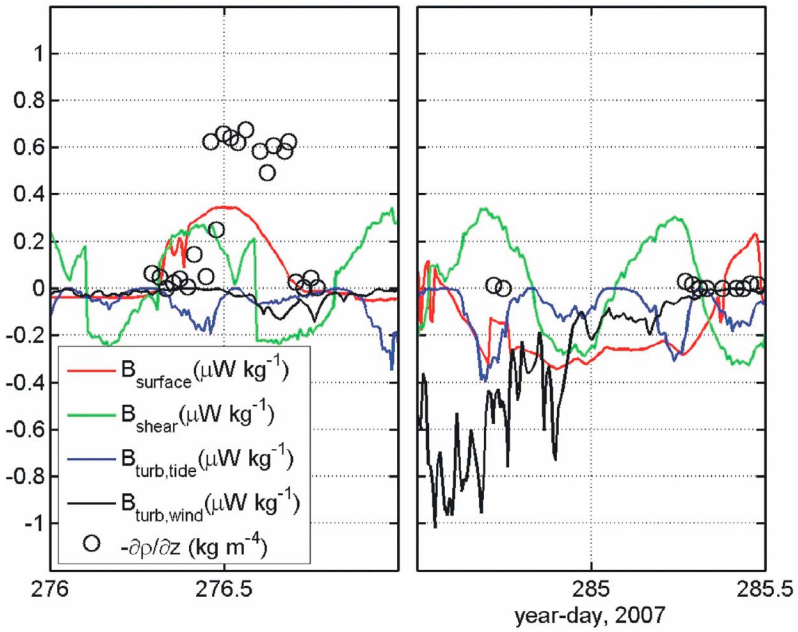

Figure 12. Two time series of estimated upper water column buoyancy fluxes and stratification at the shoal site, showing processes that can indirectly impact turbulence by modifying stratification. Shown are the stratification over the upper 2 m ($-\partial\rho/\partial z$) measured with CTD profiles and buoyancy fluxes due to surface heat flux ($B_{surface}$), tidal straining (B_{shear}), tide-driven mixing ($B_{turb,tide}$), and wind-driven mixing ($B_{turb,wind}$). (left) A sunny period is shown when there were strong positive buoyancy fluxes and restratification during ebb (year day 276.4). (right) A stormy period is shown with a fall season storm with wind-driven destratification followed by strong overnight heat loss and no restratification on the morning ebb (year day 285.2).

event. Strong stratification of 1 kg m^{-4} returned on the ebb tide during the sunny afternoon of year day 285.

5.5. Indirect Impacts of Heat Flux on Near-Surface Turbulence Generation

[68] The buoyancy flux analysis above, as well as the significant correlations between Q_{net} and ε_{50}, suggests a possible role for air-sea heat fluxes in turbulence generation. Our turbulence data set is unusual in that it includes full diurnal cycles and stormy periods that help evaluate this role: most prior estuary studies with dissipation measurements have only sampled during the daytime and relatively calm conditions [e.g., *Peters and Bokhorst*, 2000; *Zappa et al.*, 2003], and this highlights the utility of an autonomous turbulence sampling platform.

[69] The mechanism for decreased turbulence during periods with a downward net heat flux (e.g., a negative Q_{net},, on a sunny warm day) is most likely enhanced temperature stratification, damping turbulence (e.g., Figure 12). As mentioned in section 4, temperature was frequently an important contributor to the full water column vertical density gradient, and at times had the same importance as salinity in near-surface stratification, doubling stratification and the gradient Richardson number on some sunny afternoons (e.g., year day 276 [*Orton et al.*, 2010a]).

[70] Possible mechanisms for enhanced turbulence due to surface cooling include penetrative convection, and increased shear instability due to reductions in stratification (section 5.4). In lakes, surface heat loss is an important factor for turbulence, with seasonal or diurnal convective overturning [*Imberger*, 1985]. Also, in detailed studies of the sea surface, it has been shown that skin layer recovery after a disturbance occurs more rapidly when there is an upward surface heat flux [*Zappa et al.*, 1998]. The observed overnight mean 510 W m^{-2} heat flux only directly provides a buoyancy flux out of the upper water column of $B_{surface}$ = 3×10^{-7} W kg^{-1} (equation (12) and Figure 8). This is the maximum buoyancy production of TKE that could occur, and thus puts a ceiling on the TKE dissipation resulting from convection. Additionally, a surface flux does not have any direct impact on the TKE budget unless the water becomes negatively buoyant to the degree that gravitational forces can overcome viscous ones and buoyancy production of TKE can occur. Therefore, the correlation between ε_{50} and Q_{net} does not appear to be a direct result of cooling-induced convection.

[71] The highest ε_{50} values of the study were observed during a moderate ebb tide from year day 285.14–285.31, in spite of mean northwest winds below 5 m s^{-1}. CTD profiling was performed manually on site from year day 285.25 onward, showing weak stratification (Figure 12), and the ADV was verified to be working without obstruction. It is likely that the low stratification resulting from the storm was an important factor, and that processes related to forced convection at a density front or due to wind straining of a cross-estuary density gradient are likely to have provided the energy for the strong ε_{50}. Closer examination of short timescale ε (~30 s averages), 2 Hz wind and temperature

data, and 1 Hz ADCP velocity and backscatter profiles have so far been inconclusive, but it involved less than ~1% of the ε_{50} data and further analyses are beyond the scope of this paper.

[72] The Chesapeake also exhibits a "temperature inversion" in fall, where temperature opposes the salinity stratification, and was observed to be directly responsible for a 20–25% decrease in stratification early in the fall season, priming the system for increased mixing during fall storms [*Blumberg and Goodrich*, 1990]. A model experiment adding and removing the temperature inversion found that the inversion was important in the completeness of estuary deep water mixing, as well as its abruptness, but not in the timing of the event [*Blumberg and Goodrich*, 1990].

[73] It is likely that the correlation between Q_{net} and ε_{50} would be reduced during periods with larger freshwater inputs to the estuary such as the spring freshet, when along-estuary salinity gradients are larger and tidal straining is stronger. However, the observed heat fluxes were not unusual for sunny weather or fall season cooling events, and the along-estuary density gradient observed during the study was not unusual compared with prior observations in the Chesapeake [e.g., *Blumberg and Goodrich*, 1990; *Scully et al.*, 2005], Delaware Bay [*Chen and Sanford*, 2009], or San Francisco Bay [*Stacey et al.*, 2001; *Stacey and Ralston*, 2005].

6. Summary and Conclusions

[74] An experiment was performed on the Hudson River Estuary to study the influence of water column and atmospheric processes on near-surface turbulence, and to demonstrate a framework for making autonomous measurements of these processes. Analyses of the forcing of near-surface TKE dissipation (ε_{50}) from the air- and water-side suggest that wind is the primary driver of the turbulence, but significant positive correlations also exist for ε_{50} and surface water speed (u_{50}), as well as net upward air-sea heat flux (Q_{net}).

[75] A weaker correlation was found between ε_{50} and bed stress, suggesting that simple bed stress wall layer or open-channel flow models are not likely to be useful for predicting near-surface turbulence or gas exchange. This is because stratification in a partially mixed or salt wedge estuary can have complex effects due to its impact of damping turbulence but also accompanying and promoting enhanced shear on ebb tides, leading to local shear instability high in the water column.

[76] Seeking a dynamical explanation for the positive correlation between ε_{50} and Q_{net}, processes controlling water column stratification on sunny days and stormy days were contrasted. Solar heat input and straining caused similar buoyancy fluxes and promoted ebb tide restratification on a sunny day. Wind-driven mixing dominated during a fall season storm event, but strong overnight heat loss after the storm appeared to help prevent restratification during an ebb tide afterward.

[77] The near-surface TKE budget at a shallow shoal study site was closed for a strong spring ebb tides, but turbulence was weak and estimated TKE terms noisy for spring floods. Looking to spring tide data from a deep channel site for a better signal-to-noise ratio, a local TKE budget between P and ε was not valid in the upper half of the water column, because the turbulent TKE transport term is of a similar magnitude to P. However, both terms are small relative to spring tide ebb shear production values. Near-surface turbulence was generally stronger on ebb tides than floods, and this is related to the dynamics of partially mixed and salt wedge estuaries that lead to shear throughout the water column on ebbs, but low shear in the upper water column on floods. Shear production and upward turbulent transport of TKE during spring ebbs add TKE to the upper water column, whereas spring floods exhibit a well-defined bottom boundary layer and low shear production in the upper water column.

[78] In an era where the influence of air-sea interaction processes on estuarine and coastal flows are increasingly being appreciated, improved observational tools should be utilized to measure wind-driven momentum fluxes, air-sea heat exchanges, and wind-driven mixing. The dual observation approach demonstrated in this study, with bottom profiler and surface catamaran based turbulence and air-sea exchange observations, provides the opportunity to collect detailed autonomous measurements of these processes. Future studies can improve on our approach with either direct eddy covariance or atmospheric profile based flux estimates of heat and momentum exchanges [*McGillis et al.*, 2001], the latter method of which has been used on subsequent deployments of the catamaran. A fully integrated atmosphere-ocean measurement approach holds great promise for improving our understanding of the effects of atmospheric processes on near-surface turbulence across the coastal zone.

[79] **Acknowledgments.** The authors would like to thank Rich Pawlowicz and Bob Beardsley for their highly useful Matlab air-sea toolbox. Research was funded by the Hudson River Foundation with a graduate fellowship and by the National Science Foundation through grant 0526677 and a GK-12 fellowship in the program "Learning through Earth & Environmental Field Studies."

References

Blumberg, A., and D. Goodrich (1990), Modeling of wind-induced destratification in Chesapeake Bay, *Estuaries Coasts*, *13*(3), 236–249, doi:10.2307/1351914.

Chant, R. J., W. R. Geyer, R. Houghton, E. Hunter, and J. Lerczak (2007), Estuarine boundary layer mixing processes: Insights from dye experiments, *J. Phys. Oceanogr.*, *37*(7), 1859–1877, doi:10.1175/JPO3088.1.

Chen, S.-N., and L. P. Sanford (2009), Axial wind effects on stratification and longitudinal salt transport in an idealized, partially mixed estuary, *J. Phys. Oceanogr.*, *39*(8), 1905–1920, doi:10.1175/2009JPO4016.1.

Chu, C. R., and G. H. Jirka (2003), Wind and stream flow induced reaeration, *J. Environ. Eng.*, *129*(12), 1129–1136, doi:10.1061/(ASCE)0733-9372(2003)129:12(1129).

Clark, N., L. Eber, R. Laurs, J. Renner, and J. Saur (1974), Heat exchange between ocean and atmosphere in the eastern North Pacific for 1961–71, *NOAA Tech. Rep. NMFS SSRF*, *682*, 108.

Cloern, J. (1987), Turbidity as a control on phytoplankton biomass and productivity in estuaries, *Cont. Shelf Res.*, *7*(11–12), 1367–1381, doi:10.1016/0278-4343(87)90042-2.

Drennan, W. M., P. K. Taylor, and M. J. Yelland (2005), Parameterizing the sea surface roughness, *J. Phys. Oceanogr.*, *35*(5), 835–848, doi:10.1175/JPO2704.1.

Fairall, C. W., E. F. Bradley, J. E. Hare, A. A. Grachev, and J. B. Edson (2003), Bulk parameterization of air-sea fluxes: Updates and verification for the COARE algorithm, *J. Clim.*, *16*(4), 571–591, doi:10.1175/1520-0442(2003)016<0571:BPOASF>2.0.CO;2.

Gargett, A. E., and J. R. Wells (2007), Langmuir turbulence in shallow water. Part 1. Observations, *J. Fluid Mech.*, *576*(1), 27–61, doi:10.1017/S0022112006004575.

Gemmrich, J. R., and D. M. Farmer (2004), Near-surface turbulence in the presence of breaking waves, *J. Phys. Oceanogr.*, *34*, 1067–1086, doi:10.1175/1520-0485(2004)034<1067:NTITPO>2.0.CO;2.

Geyer, W. R., and J. D. Smith (1987), Shear instability in a highly stratified estuary, *J. Phys. Oceanogr.*, *17*(10), 1668–1679, doi:10.1175/1520-0485(1987)017<1668:SIIAHS>2.0.CO;2.

Grant, H. L., R. W. Stewart, and A. Moilliet (1962), Turbulence spectra from a tidal channel, *J. Fluid Mech.*, *12*, 241–268, doi:10.1017/S002211206200018X.

Hurther, D., U. Lemmin, and E. Terray (2007), Turbulent transport in the outer region of rough-wall open-channel flows: The contribution of large coherent shear stress structures (LC3S), *J. Fluid Mech.*, *574*(1), 465–493, doi:10.1017/S0022112006004216.

Imberger, J. (1985), The diurnal mixed layer, *Limnol. Oceanogr.*, *30*, 737–770, doi:10.4319/lo.1985.30.4.0737.

Ivey, G., and J. Imberger (1991), On the nature of turbulence in a stratified fluid. I, The energetics of mixing, *J. Phys. Oceanogr.*, *21*(5), 650–658, doi:10.1175/1520-0485(1991)021<0650:OTNOTI>2.0.CO;2.

Jay, D. A., and E. P. Flinchem (1999), A comparison of methods for analysis of tidal records containing multi-scale non-tidal background energy, *Cont. Shelf Res.*, *19*(13), 1695–1732, doi:10.1016/S0278-4343(99)00036-9.

Josey, S., D. Oakley, and R. Pascal (1997), On estimating the atmospheric longwave flux at the ocean surface from ship meteorological reports, *J. Geophys. Res.*, *102*, 27,961–27,972, doi:10.1029/97JC02420.

Li, M., L. Zhong, and W. C. Boicourt (2005), Simulations of Chesapeake Bay estuary: Sensitivity to turbulence mixing parameterizations and comparison with observations, *J. Geophys. Res.*, *110*, C12004, doi:10.1029/2004JC002585.

Lu, Y., and R. G. Lueck (1999), Using a broadband ADCP in a tidal channel. Part II: Turbulence, *J. Atmos. Oceanic Technol.*, *16*(11), 1568–1579, doi:10.1175/1520-0426(1999)016<1568:UABAIA>2.0.CO;2.

Lu, Y., R. G. Lueck, and D. Huang (2000), Turbulence characteristics in a tidal channel, *J. Phys. Oceanogr.*, *30*(5), 855–867, doi:10.1175/1520-0485(2000)030<0855:TCIATC>2.0.CO;2.

Malone, T. C. (1977), Environmental regulation of phytoplankton productivity in the lower Hudson Estuary, *Estuarine Coastal Mar. Sci.*, *5*(2), 157–171, doi:10.1016/0302-3524(77)90014-7.

McGillis, W. R., J. B. Edson, J. D. Ware, J. W. H. Dacey, J. E. Hare, C. W. Fairall, and R. Wanninkhof (2001), Carbon dioxide flux techniques performed during GasEx-98, *Mar. Chem.*, *75*, 267–280, doi:10.1016/S0304-4203(01)00042-1.

Nepf, H. M., and W. R. Geyer (1996), Intratidal variations in stratification and mixing in the Hudson estuary, *J. Geophys. Res.*, *101*, 12,079–12,086, doi:10.1029/96JC00630.

Nimmo Smith, W. A. M., S. A. Thorpe, and A. Graham (1999), Surface effects of bottom-generated turbulence in a shallow tidal sea, *Nature*, *400*, 251–254, doi:10.1038/22295.

Orton, P. M. (2010), Estuary turbulence and air-water CO_2 exchange, Ph.D. Dissertation thesis, 211 pp, Columbia Univ., New York.

Orton, P. M., and G. Kineke (2001), Comparing calculated and observed vertical suspended-sediment distributions from a Hudson River Estuary turbidity maximum, *Estuarine Coastal Shelf Sci.*, *52*(3), 401–410, doi:10.1006/ecss.2000.0747.

Orton, P. M., and M. Visbeck (2009), Variability of internally generated turbulence in an estuary, from 100 days of continuous observations, *Cont. Shelf Res.*, *29*(1), 61–77, doi:10.1016/j.csr.2007.07.008.

Orton, P. M., W. R. McGillis, and C. J. Zappa (2010a), Sea breeze forcing of estuary turbulence and CO_2 exchange, *Geophys. Res. Lett.*, *37*, L13603, doi:10.1029/2010GL043159.

Orton, P. M., C. J. Zappa, and W. R. McGillis (2010b), An autonomous self-orienting catamaran (SOCa) for measuring air-water fluxes and forcing, in *Gas Transfer at Water Surfaces*, edited by S. Komori et al., Kyoto Univ. Press, Kyoto, Japan, in press.

Peters, H. (1999), Spatial and temporal variability of turbulent mixing in an estuary, *J. Mar. Res.*, *57*, 805–845, doi:10.1357/002224099321514060.

Peters, H., and R. Bokhorst (2000), Microstructure observations of turbulent mixing in a partially mixed estuary. Part I: Dissipation rate, *J. Phys. Oceanogr.*, *30*, 1232–1244, doi:10.1175/1520-0485(2000)030<1232:MOOTMI>2.0.CO;2.

Pulkkinen, K. (1993), Comparison of different bin-mapping methods for a bottom-mounted acoustic profiler, *J. Atmos. Oceanic Technol.*, *10*(3), 404–409, doi:10.1175/1520-0426(1993)010<0404:CODBMM>2.0.CO;2.

Reed, R. (1977), On estimating insolation over the ocean, *J. Phys. Oceanogr.*, *7*(3), 482–485, doi:10.1175/1520-0485(1977)007<0482:OEIOTO>2.0.CO;2.

Rippeth, T. P., M. R. Palmer, J. H. Simpson, N. R. Fisher, and J. Sharples (2005), Thermocline mixing in summer stratified continental shelf seas, *Geophys. Res. Lett.*, *32*, L05602, doi:10.1029/2004GL022104.

Schumann, U., and T. Gerz (1995), Turbulent mixing in stably stratified shear flows, *J. Appl. Meteorol.*, *34*(1), 33–48, doi:10.1175/1520-0450-34.1.33.

Scully, M., C. Friedrichs, and J. Brubaker (2005), Control of estuarine stratification and mixing by wind-induced straining of the estuarine density field, *Estuaries Coasts*, *28*(3), 321–326, doi:10.1007/BF02693915.

Scully, M., W. Geyer, and J. Trowbridge (2010), The influence of stratification and non-local turbulent production on estuarine turbulence: An assessment of turbulence closure with field observations, *J. Phys. Oceanogr.*, doi:10.1175/2010JPO4470.1, in press.

Scully, M. E., W. R. Geyer, and J. A. Lerczak (2009), The Influence of Lateral Advection on the Residual Estuarine Circulation: A Numerical Modeling Study of the Hudson River Estuary, *J. Phys. Oceanogr.*, *39*(1), 107–124, doi:10.1175/2008JPO3952.1.

Simpson, J., J. Brown, J. Mathews, and G. Allen (1990), Tidal straining, density currents, and stirring in the control of estuarine stratification, *Estuaries*, *13*, 125–132, doi:10.2307/1351581.

Simpson, J., W. Crawford, T. Rippeth, A. Campbell, and J. Cheok (1996), The vertical structure of turbulent dissipation in shelf seas, *J. Phys. Oceanogr.*, *26*(8), 1579–1590, doi:10.1175/1520-0485(1996)026<1579:TVSOTD>2.0.CO;2.

Souza, A. J., N. R. Fisher, J. H. Simpson, and M. J. Howarth (2008), Effects of tidal straining on the semidiurnal cycle of dissipation in the Rhine region of freshwater influence: Comparison of model and measurements, *J. Geophys. Res.*, *113*, C01011, doi:10.1029/2006JC004002.

Stacey, M. T. (2003), Estimation of diffusive transport of turbulent kinetic energy from acoustic Doppler current profiler data, *J. Atmos. Oceanic Technol.*, *20*(6), 927–935, doi:10.1175/1520-0426(2003)020<0927:EODTOT>2.0.CO;2.

Stacey, M. T., and D. K. Ralston (2005), The scaling and structure of the estuarine bottom boundary layer, *J. Phys. Oceanogr.*, *35*(1), 55–71, doi:10.1175/JPO-2672.1.

Stacey, M. T., S. G. Monismith, and J. R. Burau (1999), Measurements of Reynolds stress profiles in unstratified tidal flow, *J. Geophys. Res.*, *104*, 10,933–10,949, doi:10.1029/1998JC900095.

Stacey, M. T., J. R. Burau, and S. G. Monismith (2001), Creation of residual flows in a partially stratified estuary, *J. Geophys. Res.*, *106*, 17,013–17,037, doi:10.1029/2000JC000576.

Tennekes, H., and J. L. Lumley (1972), *A First Course in Turbulence*, MIT Press, Cambridge, Mass.

Veron, F., and W. K. Melville (1999), Pulse-to-pulse coherent Doppler measurements of waves and turbulence, *J. Atmos. Oceanic Technol.*, *16*, 1580–1597, doi:10.1175/1520-0426(1999)016<1580:PTPCDM>2.0.CO;2.

Voulgaris, G., and J. H. Trowbridge (1998), Evaluation of the acoustic Doppler velocimeter (ADV) for turbulence measurements, *J. Atmos. Oceanic Technol.*, *15*, 272–289, doi:10.1175/1520-0426(1998)015<0272:EOTADV>2.0.CO;2.

Warner, J. C., W. R. Geyer, and J. A. Lerczak (2005), Numerical modeling of an estuary: A comprehensive skill assessment, *J. Geophys. Res.*, *110*, C05001, doi:10.1029/2004JC002691.

Zappa, C. J., A. T. Jessup, and H. H. Yeh (1998), Skin-layer recovery of free-surface wakes: Relationship to surface renewal and dependence on heat flux and background turbulence, *J. Geophys. Res.*, *103*(C10), 21,711–21,722, doi:10.1029/98JC01942.

Zappa, C. J., P. A. Raymond, E. Terray, and W. R. McGillis (2003), Variation in surface turbulence and the gas transfer velocity over a tidal cycle in a macro-tidal estuary, *Estuaries*, *26*(6), 1401–1415, doi:10.1007/BF02803649.

Zappa, C. J., W. R. McGillis, P. A. Raymond, J. B. Edson, E. J. Hintsa, H. J. Zemmelink, J. W. H. Dacey, and D. T. Ho (2007), Environmental turbulent mixing controls on air-water gas exchange in marine and aquatic systems, *Geophys. Res. Lett.*, *34*, L10601, doi:10.1029/2006GL028790.

W. R. McGillis, Earth and Environmental Engineering, Columbia University, New York, NY 10027, USA.

P. M. Orton, Stevens Institute of Technology, Babbio Building, Castle Point on Hudson, Hoboken, NJ 07030, USA. (philip.orton@stevens.edu)

C. J. Zappa, Lamont-Doherty Earth Observatory of Columbia University, 61 Route 9W, Palisades, NY 10964, USA.